Catalysis Letters (2021) 151:2228–2236
https://doi.org/10.1007/s10562-020-03470-y

Ni–Mo–S Ternary Chalcogenide Thin Film for Enhanced Hydrogen Evolution Reaction

Cihan Kuru[1,3] · **Mirac Alaf**[1,3] · **Yunus E. Simsek**[2,3]

Received: 16 September 2020 / Accepted: 17 November 2020 / Published online: 2 January 2021

Abstract

Transition metal dichalcogenides (TMDs) hold a great promise to replace Pt-based catalysts for hydrogen evolution reaction (HER). Among those, MoS_2 has been the center of attention. In this work, we investigate the effect of Ni addition on the catalytic activity of MoS_2 thin film in HER. Ni–Mo–S ternary chalcogenide thin films with varying Ni concentrations were fabricated by a two-step process: co-sputtering of Ni-Mo alloy films and thermal sulfurization. The HER performance of MoS_2 (620 mV overpotential and 138 mV dec^{-1} Tafel slope) is surpassed by the resulting ternary chalcogenides, among which the Ni–Mo–S film at 50 at.% Ni concentration exhibits the highest catalytic activity with an overpotential of 400 mV at 10 mA cm^{-2} and Tafel slope of 81 mV dec^{-1}. The Ni addition promotes HER kinetics by altering the morphology and electronic structure of MoS_2 thin film, leading to improved H^+ ion adsorption, reduced charge transfer resistance and increased electrochemical surface area. This study provides a method for the controllable fabrication of ternary chalcogenide thin films and paves the way for the exploration of new combinations of ternary TMDs.

Graphic Abstract

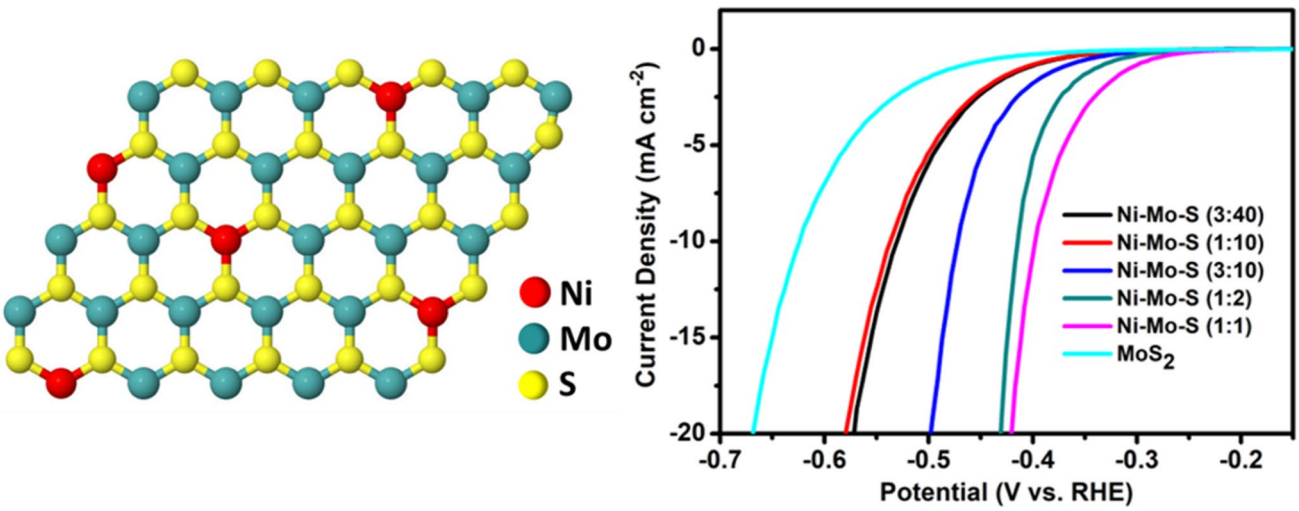

Keywords Ni · Ternary chalcogenides · MoS_2 · Hydrogen evolution reaction · Catalyst · TMDs

1 Introduction

The growing energy demand [1] and the environmental problems caused by fossil fuels [2] necessitates the wider exploitation of renewable energy sources. Hydrogen is a

Supplementary information The online version of this article (https://doi.org/10.1007/s10562-020-03470-y) contains supplementary material, which is available to authorized users.

✉ Cihan Kuru
cihan.kuru@bilecik.edu.tr

Extended author information available on the last page of the article

promising alternative to fossil fuels and considered as a clean fuel if produced from water splitting using renewable energy [3]. One encouraging approach to produce hydrogen is to employ electrochemical hydrogen evolution where the energy input is supplied by renewable sources such sun, wind or hydropower [4]. Thus, the excess renewable energy can be stored as hydrogen, preventing energy wastage and later can be converted to electricity in a fuel cell.

Catalysts are used to minimize the energy required to split water into hydrogen and oxygen [5–7]. Up to date, Pt has been proved to be the most active catalyst for HER; however, Pt is a scarce metal with high cost, which impedes its use in large scale [8]. Hence, developing low-cost, earth abundant and robust catalysts that have comparable activity to Pt is a critical step in transition to hydrogen economy. TMDs offer exciting opportunities due to their unique electronic, optical and chemical properties [9–11]. TMDs have become the potential candidates to replace Pt-based catalysts [12–15]. Among them, MoS_2 has received massive attention owing to its hopeful catalytic properties and excellent stability in acidic medium [16–19]. However, the catalytic activity of MoS_2 is limited by its poor electrical conductivity and inactive basal plane [20, 21]. Great effort has been devoted to improving the catalytic activity of MoS_2. Creating defects on the basal plane of MoS_2 [22], coupling MoS_2 with graphene [23], decorating MoS_2 surface with metal nanoparticles [24], synthesizing metallic phase MoS_2 [25] and fabricating atomically thin MoS_2 nanosheets [26] have been shown to enhance the HER performance.

The physicochemical properties of the TMDs can be dramatically changed with the incorporation of a third element. The charge distribution of in-plane S atoms can be modulated by the amount of solute atoms to result in the optimum Gibbs free energy of hydrogen adsorption (ΔG_H) for HER. Moreover, a doping effect may be induced because the solute atom has a different valency than host atom, which leads to increased electrical conductivity. Ni incorporation has been demonstrated to effectively modify the electronic structure of MoS_2 and thus enhance the catalytic activity in HER [27–29]. Considering these potential benefits, we fabricated Ni–Mo–S ternary chalcogenide thin films with varying Ni/Mo ratios by co-sputtering and ensuing thermal sulfurization step. The Ni–Mo–S thin films with good homogeneity as well as controlled thickness and composition could be achieved. Thin film geometry of the catalysts enabled us to study the intrinsic activity of the Ni–Mo–S films while mitigating the morphological effects, which could result in dramatic variations in surface area. The physical and chemical properties of the films were investigated by X-ray diffraction (XRD), Raman spectroscopy, X-ray photoelectron spectroscopy (XPS), energy dispersive X-ray spectroscopy (EDX) and scanning electron microscopy (SEM). Electrochemical measurements were performed to reveal the catalytic properties of the catalyst films. The results show that Ni addition into MoS_2 substantially enhances the HER performance by lowering the onset potential and Tafel slope, which stemmed from the modification of the electronic structure and morphology of MoS_2.

2 Experimental Methods

2.1 Sputter Deposition of Ni–Mo Alloy Films

Ni–Mo alloy films were prepared in a multi-target sputtering system (Vaksis Angora). Ni and Mo targets (99.9% purity, Kurt Lesker) were simultaneously sputtered to form 20 nm thick Ni-Mo alloy films on n^+ Si (100) substrates. Prior to deposition, the substrates were cleaned in acetone and isopropyl alcohol using an ultrasonic bath, followed by the etching of natural oxide layer on Si by diluted HF, rinsing in deionized water and drying with N_2 gas blow. Once the substrates were loaded in the sputter chamber, the chamber was evacuated to 5×10^{-6} Torr and filled with Ar gas with a pressure of 10 mTorr. Ni/Mo atomic ratio was controlled by adjusting the sputter power of each target. The detailed description of the process is given in the supplementary material (Fig. S1, Table S1). At each run, target surfaces were cleaned by pre-sputtering for 5 min while keeping shutters closed. The substrate holder was rotated at 5 rpm to ensure film uniformity.

2.2 Thermal Sulfurization of the Ni–Mo Alloy Films

The deposited Ni–Mo alloy films were subjected to thermal sulfurization process in a tube furnace (MTI OTF-1200X-S-NT-LD) equipped with a 2-inch diameter quartz tube having a gas inlet and outlet (Fig. 1). The samples were situated at the center of the tube while 0.5 g sulfur powder (Merck Millipore) at the upstream side. The tube was flashed with high purity N_2 gas (99.999% purity) for 1 h to remove oxygen present inside the tube. Then, the temperature of the furnace was ramped up to 600 °C in 60 min and kept at the reaction temperature for 20 min before naturally cooled down to ambient temperature, during which the N_2 flow with a rate of 100 s.c.c.m. was maintained. The temperature of the sulfur powder was about 150 °C during the reaction.

2.3 Characterization

SEM and EDX mapping micrographs were obtained with FEI Quanta FEG 450 scanning electron microscope. Grazing angle XRD measurements were carried out with Rigaku D-Max with Cu-Kα source (1.54 Å). XPS data were collected on SPECS FlexMod using Al-Kα radiation source (1486.71 eV). Binding energies were calibrated against the C 1 s peak using the

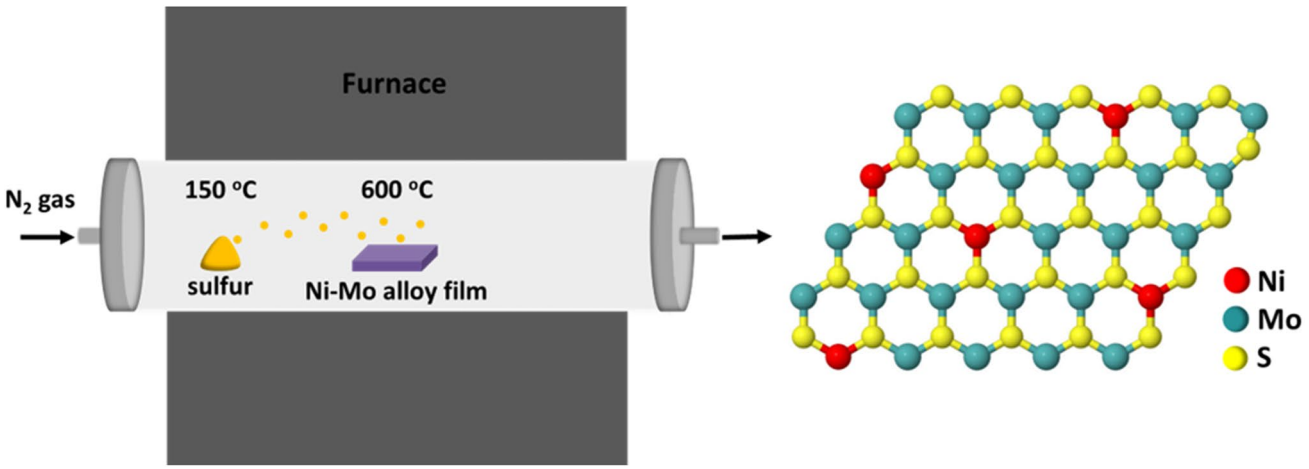

Fig. 1 Schematic illustration of the fabrication of the Ni–Mo–S ternary chalcogenide thin films

reference value of 284.5 eV. Raman spectroscopy measurements were conducted by WITech alpha 300R with a wavelength of 532 nm. The thickness of the films was determined with a profilometer (Terralab).

2.4 Electrochemical Measurements

After scratching the backside of the Si substrates, an electrical contact was made to form the working electrodes using silver epoxy and a piece of copper wire. Chemically inert epoxy (Hysol 3423) was used to define an active area of 0.2–0.4 cm^2 for the electrochemical measurements. The electrochemical measurements were conducted in 0.5 M H_2SO_4 solution using Gamry Interface 1000 potentiostat with a three-electrode setup consisting of the working electrode, Ag/AgCl (3 M NaCl) reference electrode and Pt coil counter electrode. The electrolyte was purged with N_2 gas and stirred at 750 rpm during the measurements. The reference electrode potential was converted to reversible hydrogen electrode (RHE) potential using the relation $E(RHE) = E(Ag/AgCl) + 0.209V$. Linear sweep voltammetry measurements were performed at a scan rate of 5 mV s^{-1}. The data have been corrected for ohmic drop using Gamry software. Impedance measurements were recorded within the frequency range of 0.1 Hz–100 kHz at 400 mV overpotential with an excitation voltage of 10 mV. Stability measurements were conducted by 1000 cycles of CV scans performed between − 0.2 to (− 0.6) V versus Ag/AgCl with a scan rate of 50 mV s^{-1}.

3 Results and Discussion

The thickness of the sulfurized Ni-Mo alloy films was found to be about 30 nm. The crystal structure of the synthesized catalyst films was investigated by XRD analysis. The XRD patterns of the sulfurized Mo, Ni, Ni-Mo (3:10) and Ni-Mo (1:1) alloy films are displayed in Fig. 2a. The Mo film sulfurized at 800 °C exhibits peaks corresponding to (002), (100), (101) and (110) planes, indicating hexagonal MoS_2 crystal structure (PDF#01-075-1539). On the other hand, the XRD pattern of the Mo film sulfurized at 600 °C matches well with monoclinic MoO_2 phase (PDF#00-032-0671). The Mo film is considered to react with trace amount of oxygen present in the carrier gas to form MoO_3, which then is reduced to MoO_2 after reacting with elemental sulfur. Unlike the reaction occurring at 800 °C, the conversion of the film into MoS_2 did not take place at 600 °C most likely by virtue of inadequate temperature. On the other hand, the Ni-Mo (3:10) and Ni-Mo (1:1) alloy films sulfurized at 600 °C both show MoS_2 phase. Additionally, the films contain small amount of secondary phases including NiO (PDF#01–073-1523) and NiS (PFD#01–089-1955) as indicated by the corresponding ambiguous peaks. The (002) peak was observed to become prominent after the Ni addition. TMDs have a layered structure and the (002) peak is associated with horizontally aligned layers [30]. Since the intensity of the (002) peak increases with the Ni addition, we infer that Ni promotes horizontal layer stacking. Moreover, the position of the (002) peak slightly shifted to larger angle with increasing Ni content, as a result of the contraction of the interlayer spacing (Fig. 2b). These results imply that Ni atoms are successfully incorporated in the MoS_2 lattice. Furthermore, we found that the sulfurization of pure Ni film at 600 °C led to Ni_3S_2 (PDF#01-071-1682) with poor crystallinity.

The effect of Ni on the morphology of the MoS_2 film was examined by SEM. The SEM images of the MoS_2 and Ni–Mo–S (1:1) films are compared in Fig. 3a and b, in which the MoS_2 has a quite flat surface while the Ni–Mo–S (1:1)

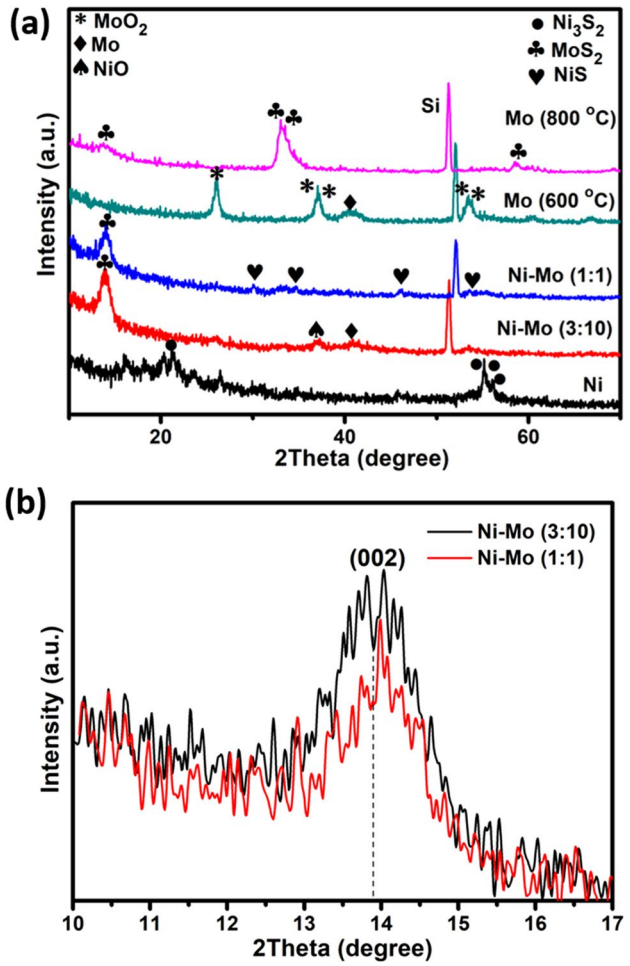

Fig. 2 **a** XRD patterns of the sulfurized Mo, Ni, Ni-Mo (3:10) and Ni-Mo (1:1) alloys films. **b** Close-up of the (002) peak of the sulfurized Ni-Mo (3:10) and Ni-Mo (1:1) alloy films

exhibits a granular structure consisting of irregular-sized grains. The EDX mapping of S, Ni and Mo clearly indicates a uniform elemental distribution (Fig. 3c).

Raman spectra of the MoS_2 and Ni–Mo–S (1:1) films are exhibited in Fig. 4a, in which both films display the characteristic in-plane E^1_{2g} and out-of-plane A_{1g} vibrational modes of MoS_2 [31]. Note that the peak at 518 cm^{-1} is originated from the Si substrate [32]. No peaks related to Ni-S compounds have been detected, confirming that the MoS_2 crystal structure is preserved after the Ni addition. In addition, the E^1_{2g} and A_{1g} peaks shifts to lower wavenumbers, suggesting that Ni incorporation induced n-type doping in the MoS_2 (Fig. 4b) [33]. The E^1_{2g} and A_{1g} peaks of the Ni–Mo–S (1:1) are broadened compared to the MoS_2 due to increased number of defect sites [34]. The intensity ratio of E^1_{2g} to A_{1g} can be used to evaluate the degree of edge termination [35]. The ratio increases from 0.30 to 0.32 with the Ni addition, pointing out less edge termination, which is consistent with the XRD results.

XPS studies were carried out to further confirm the chemical composition and reveal the chemical states of the catalyst films. The survey scans show the presence of Mo, S, O and C for both the MoS_2 and Ni–Mo–S (1:1) films (Fig. 5a). The ternary chalcogenide film exhibits an additional peak corresponding to Ni, signifying the successful incorporation of Ni into the MoS_2. The high resolution XPS scans of the Ni–Mo–S (1:1) are given in Fig. 5b–d. Two peaks of Mo 3d was detected at 229.1 and 232.0 eV (Fig. 5b), which can be assigned to Mo^{+4} $3d_{5/2}$ and Mo^{+4} $3d_{3/2}$ doublets [36]. The peak at 226.2 eV is resulted from the S 2s orbitals. The lack of Mo^{+6} $3d_{3/2}$ peak indicates no oxide formation [37]. Another doublet observed at 161.8 and 163.0 eV (Fig. 5c) is related to S $2p_{3/2}$ and S $2p_{1/2}$, indicating the -2 oxidation state of sulfur [38]. The high-resolution Ni scan (Fig. 5d) reveals two major peaks at 855.5 and 873.7 eV and satellite peaks, which corresponds to Ni^{+2} $2p_{3/2}$ and Ni^{+2} $2p_{1/2}$ [39].

Linear sweep voltammetry measurements were performed to evaluate the catalytic performance of the synthesized films. The polarization curves of the MoS_2 and Ni–Mo–S ternary chalcogenide films are depicted in Fig. 6a. The Ni_3S_2 film was not stable enough to obtain a polarization curve as it rapidly dissolved in the H_2SO_4 solution. Compared to the MoS_2, the Ni–Mo–S films show superior activity in HER, Ni–Mo–S (1:1) being the most active catalyst indicated by the lowest onset potential and highest current density (Table 1). The MoS_2 film requires an overpotential of 620 mV to reach the benchmarking current density of 10 mA cm^{-2} whereas the Ni–Mo–S (1:1) needs only 400 mV (Fig. 6b).

Tafel plots were constructed to reveal the kinetics of the HER taking place on the catalyst surface (Fig. 6c). Tafel slopes were obtained after fitting the plots to Tafel equation, $\eta = blogj + a$, where η, b, j are the overpotential, Tafel slope and current density, respectively. The Tafel slopes decrease substantially with the Ni addition, indicating faster HER kinetics. The Ni–Mo–S (1:1) film exhibits the lowest slope value of 81 mV dec^{-1}, which is much smaller than the MoS_2 (138 mV dec^{-1}). Tafel slopes between 40 and 120 mV dec^{-1} suggests that the HER occurs via Volmer-Heyrovsky mechanism [40]. The MoS_2 has a Tafel slope around 120 mV dec^{-1}, which implies the rate determining step of Volmer reaction [20]. On the other hand, the Ni–Mo–S films possess Tafel slopes values ranging from 81 to 95 mV dec^{-1}, indicating that the adsorption of the H^+ ions on the surface of the catalyst is improved. For an ideal catalyst, the Gibbs free energy for hydrogen

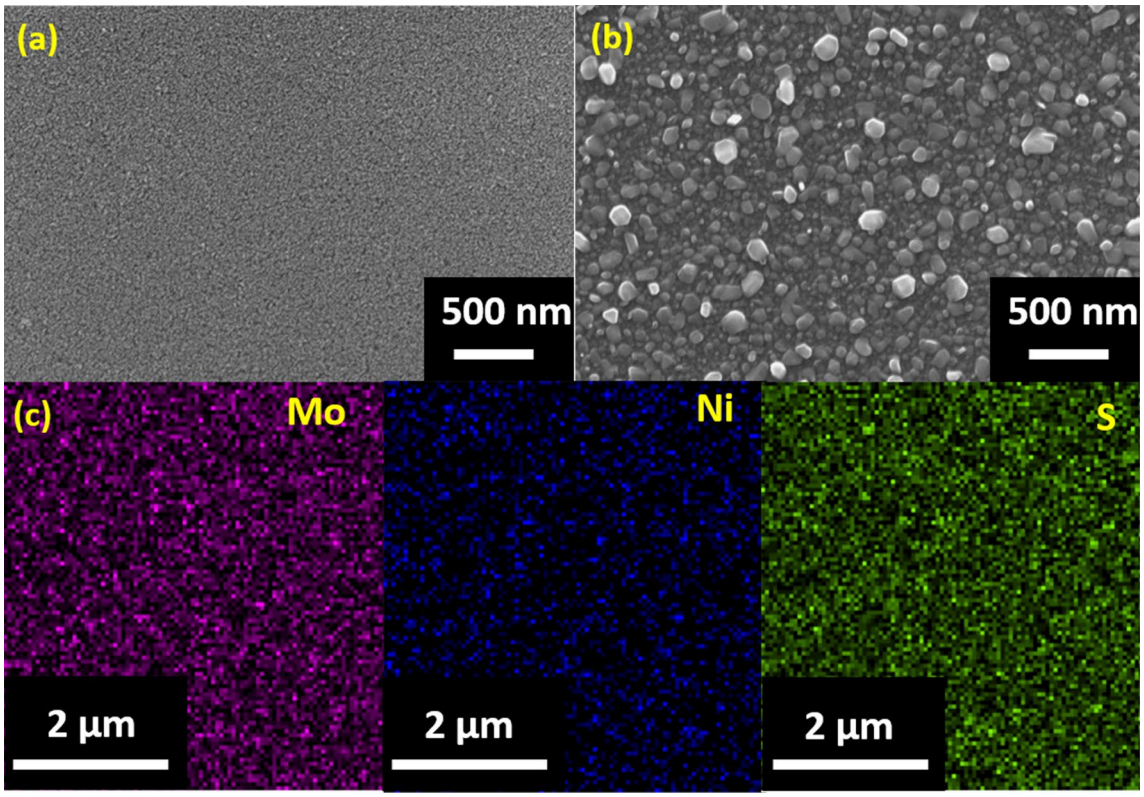

Fig. 3 SEM images of the **a** MoS_2 and **b** Ni–Mo–S (1:1) films. **c** EDX mappings of Mo, Ni and S

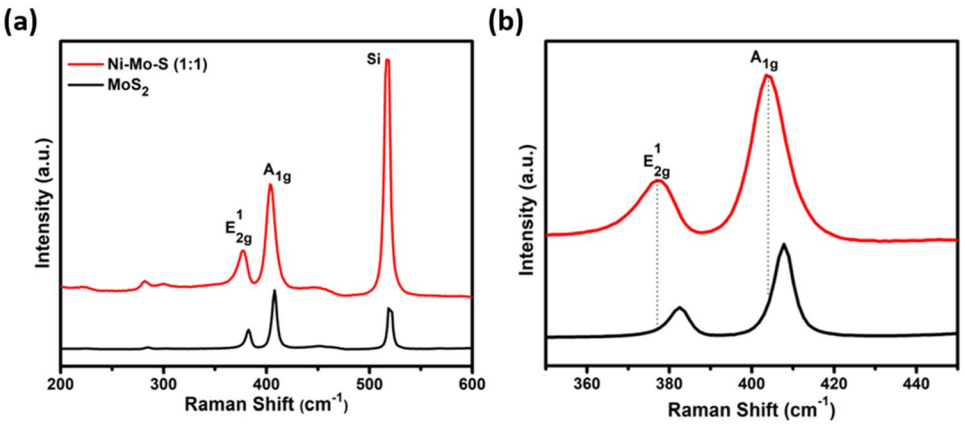

Fig. 4 **a** Raman spectra of the MoS_2 and Ni–Mo–S (1:1) films. **b** Close-up of the E^1_{2g} and A_{1g} peaks

adsorption (ΔG_H) should be close to zero [17]. The basal plane of the MoS_2 is catalytically inactive because H^+ ions cannot be effectively adsorbed on in-plane S sites due to high positive ΔG_H value (+ 1.92 eV) [21]. The Ni incorporation into the MoS_2 lattice modifies the charge distribution on the S atoms favorably, lowering the ΔG_H, in turn enhancing the HER activity of the basal plane [27]. As more Ni atoms are introduced into the lattice, more S atoms are affected, leading to increasing HER activity. In addition, granular morphology of the Ni–Mo–S ternary chalcogenide films also plays a role in the increased catalytic activity since the curved surface of the nanograins

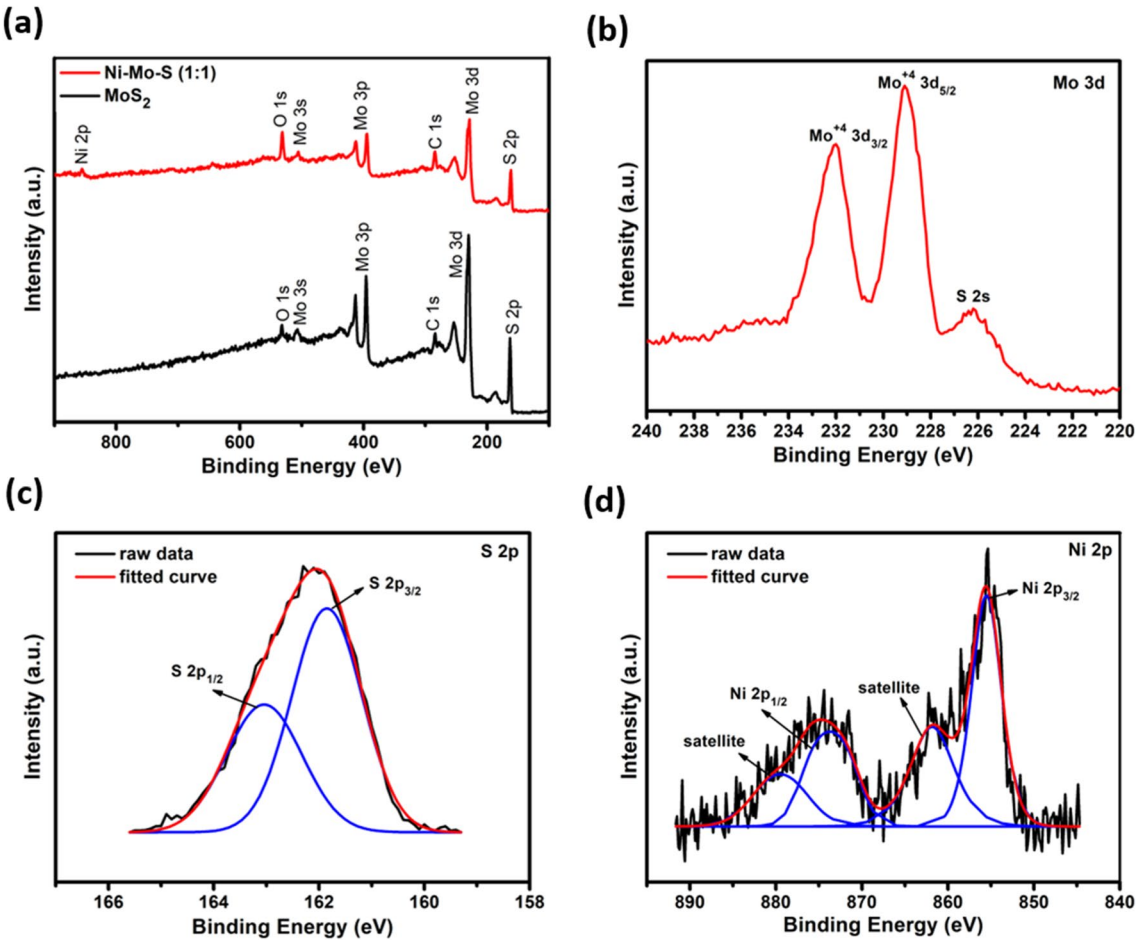

Fig. 5 **a** XPS survey spectra of the MoS_2 and Ni–Mo–S (1:1) films. The high resolution XPS spectra of the Ni–Mo–S (1:1) film including **b** Mo 3d, **c** S 2p and **d** Ni 2p

observed in the Ni–Mo–S films impose a geometrical constraint on the surface atoms, thereby modifying the ΔG_H. Kibsgaard et al. synthesized highly ordered double-gyroid MoS_2 network with a curved surface structure and reported that high surface curvature of the catalyst exposes more edge sites, dramatically enhancing the HER activity [36].

Electrochemical impedance spectroscopy measurements were carried out at $\eta = 400$ mV to determine charge transfer resistance (R_{ct}). The corresponding Nyquist plots are shown in Fig. 6d. The Nyquist plots were fitted into a modified Randles equivalent circuit model (inset Fig. 6d) to determine the R_{ct}. Ni addition was found to reduce R_{ct} dramatically. The R_{ct} values of the Ni–Mo–S films range from 120 to 153 Ω whereas the MoS_2 film has a much larger value of 10 kΩ. The high R_{ct} of the MoS_2 film is resulted from its poor charge transport ability. However, Ni increases the conductivity of the MoS_2, in turn facilitating the charge transfer.

To further corroborate the superior HER performance of the Ni–Mo–S ternary chalcogenide films, the electrochemical surface area (ECSA) was calculated using double layer capacitance (C_{dl}). Multiple CV scans were performed at a potential window of 0.1–0.3 V vs. RHE with different scan rates (20, 40, 60, 80 and 100 mV s^{-1}) and then the difference of the capacitive current density of the forward and backwards scans (Δj) at 0.15 V vs. RHE were plotted against the scan rate (Fig. 7a). The C_{dl} values were obtained from the slope of the plots. The calculated C_{dl} values are 40 μF cm^{-2} and 5 μF cm^{-2} for the Ni–Mo–S (1:1) and MoS_2 films, respectively. The C_{dl} values are low compared to literature [41–43], which may be resulted from the planar nature of the

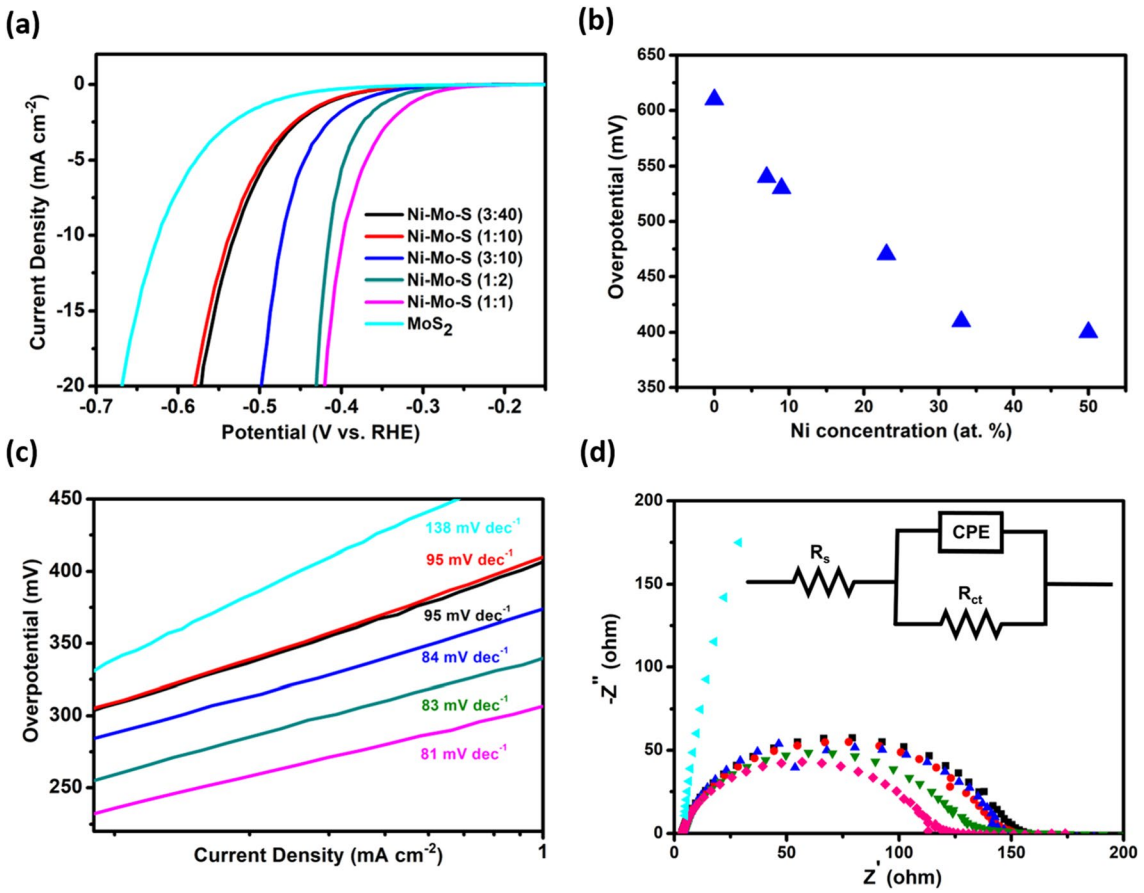

Fig. 6 **a** Polarization curves of the MoS_2 and Ni–Mo–S ternary chalcogenide films. **b** The effect of Ni concentration on the overpotential at 10 mA cm^{-2} current density. **c** Tafel plots and **d** Nyquist plots of the catalyst films

Table 1 Electrochemical HER performance of the MoS_2 and Ni–Mo–S ternary chalcogenide films

Catalyst	Tafel slope (mV/dec)	Onset potential at J = 1 mA/cm^2 (mV)	R_{ct} (ohm)
MoS_2	138	480	10,000
Ni–Mo–S (3:40)	95	410	153
Ni–Mo–S (1:10)	95	410	146
Ni–Mo–S (3:10)	84	376	146
Ni–Mo–S (1:2)	83	341	135
Ni–Mo–S (1:1)	81	306	120

films. The larger C_{dl} value of the Ni–Mo–S (1:1) film can be attributed to the increased surface roughness, as indicated by the SEM images. To exclude the effect of the surface roughness on HER performance, we normalized the polarization curves by ECSA. The normalized polarization curves are shown in Fig. 7b, in which the Ni–Mo–S (1:1) film shows notably higher HER performance than the MoS_2. Therefore, the larger ECSA of the Ni–Mo–S films cannot be solely held responsible for the enhanced HER performance.

The stability of the ternary chalcogenide film was assessed by comparing the polarization curves recorded before and after 1000 cycles of CV scans (Fig. 8). The polarization curves of the Ni–Mo–S (1:1) film show negligible difference, revealing the good stability of the catalyst film. Moreover, another set of samples show similar trend in HER performance (Fig. S2), indicating the reproducibility of the fabrication procedure.

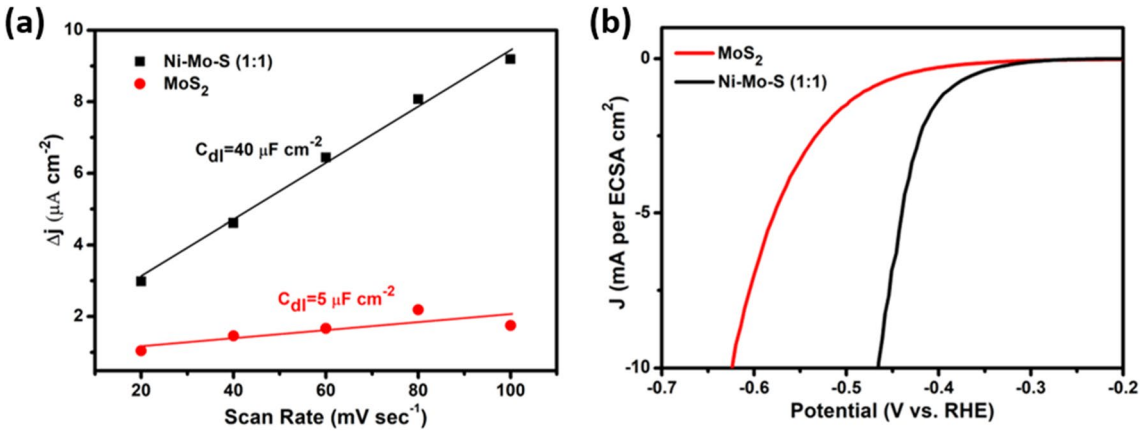

Fig. 7 **a** Estimation of double layer capacitance for the MoS_2 and Ni–Mo–S (1:1) films. **b** Polarization curves of the MoS_2 and Ni–Mo–S (1:1) films normalized by ECSA

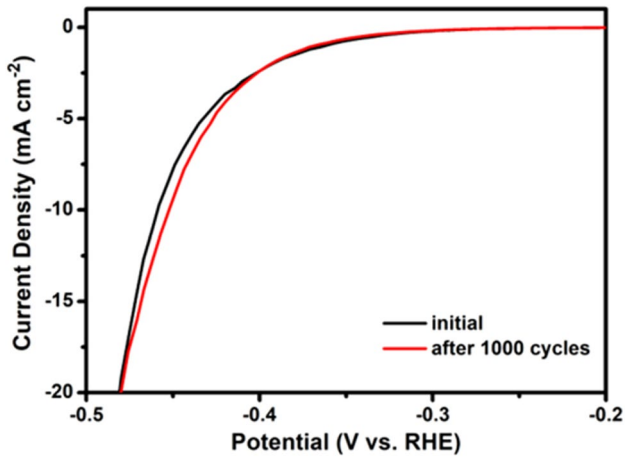

Fig. 8 Polarization curves of the Ni–Mo–S (1:1) film obtained before and after 1000 cycles of CV scans

4 Conclusion

In summary, we have demonstrated that Ni addition into MoS_2 significantly boosts the HER activity. The Ni–Mo–S ternary chalcogenide thin films having different Ni/Mo ratios were prepared by the sulfurization of the sputter deposited Ni-Mo alloy films. The XRD, EDX and XPS studies suggest the successful and homogeneous incorporation of Ni into the MoS_2 crystal. The electrochemical measurements reveal that the Ni–Mo–S(1:1) film shows the best HER performance with an overpotential of 400 mV at 10 mA cm^{-2}, a Tafel slope of 81 mV dec^{-1} and good stability over 1000 cycles of CV scans. The observed enhancement in the HER performance of the Ni–Mo–S ternary chalcogenide films is due to the combinative effects of the charge redistribution of in-plane S atoms by the Ni atoms, induced granular morphology with more edge sites, increased ECSA and improved charge transport ability.

Acknowledgements This work was supported by The Scientific and Technological Research Council of Turkey (Grand No. 117M257).

Compliance with Ethical Standards

Conflict of interest The authors declare no conflict of interests regarding the publication of this article.

References

1. Taylor P (2009) OECD.
2. Barbir F, Veziroglu T, Plassjr H (1990) Int J Hydrogen Energy 15:739–749
3. Dresselhaus MS, Thomas IL (2001) Nature 414:332–337
4. Yoshida T, Kojima K (2015) Electrochem Soc Interface 24:45–49
5. Roger I, Shipman MA, Symes MD (2017) Nat Rev Chem 1:0003
6. Du P, Eisenberg R (2012) Energy Environ Sci 5:6012
7. Zou X, Zhang Y (2015) Chem Soc Rev 44:5148–5180
8. McKone JR, Warren EL, Bierman MJ, Boettcher SW, Brunschwig BS, Lewis NS, Gray HB (2011) Energy Environ Sci 4:3573
9. Das S, Kumar C, Kumar R, Srivastava A, Jit S (2020) IEEE Photon Technol Lett 32:67–70
10. Vabbina P, Choudhary N, Chowdhury AA, Sinha R, Karabiyik M, Das S, Choi W, Pala N (2015) ACS Appl Mater Interfaces 7:15206–15213
11. Das S, Kim M, Lee J, Choi W (2014) Crit Rev Solid State Mater Sci 39:231–252
12. Yang J, Shin HS (2014) J Mater Chem A 2:5979–5985
13. Pumera M, Sofer Z, Ambrosi A (2014) J Mater Chem A 2:8981–8987
14. Gholamvand Z, McAteer D, Backes C, McEvoy N, Harvey A, Berner NC, Hanlon D, Bradley C, Godwin I, Rovetta A, Lyons MEG, Duesberg GS, Coleman JN (2016) Nanoscale 8:5737–5749
15. Gupta U, Rao CNR (2017) Nano Energy 41:49–65

16. Li G, Zhang D, Qiao Q, Yu Y, Peterson D, Zafar A, Kumar R, Curtarolo S, Hunte F, Shannon S, Zhu Y, Yang W, Cao L (2016) J Am Chem Soc 138:16632–16638
17. Hinnemann B, Moses PG, Bonde J, Jørgensen KP, Nielsen JH, Horch S, Chorkendorff I, Nørskov JK (2005) J Am Chem Soc 127:5308–5309
18. Yu Y, Huang SY, Li Y, Steinmann SN, Yang W, Cao L (2014) Nano Lett 14:553–558
19. Yang Y, Fei H, Ruan G, Xiang C, Tour JM (2014) Adv Mater 26:8163–8168
20. Huang X, Zeng Z, Zhang H (2013) Chem Soc Rev 42:1934
21. Ouyang Y, Ling C, Chen Q, Wang Z, Shi L, Wang J (2016) Chem Mater 28:4390–4396
22. Xie J, Zhang H, Li S, Wang R, Sun X, Zhou M, Zhou J, Lou XWD, Xie Y (2013) Adv Mater 25:5807–5813
23. Li Y, Wang H, Xie L, Liang Y, Hong G, Dai H (2011) J Am Chem Soc 133:7296–7299
24. Cheng Y, Lu S, Liao F, Liu L, Li Y, Shao M (2017) Adv Funct Mater 27:1700359
25. Voiry D, Salehi M, Silva R, Fujita T, Chen M, Asefa T, Shenoy VB, Eda G, Chhowalla M (2013) Nano Lett 13:6222–6227
26. Ji S, Yang Z, Zhang C, Liu Z, Tjiu WW, Phang IY, Zhang Z, Pan J, Liu T (2013) Electrochim Acta 109:269–275
27. Luo R, Luo M, Wang Z, Liu P, Song S, Wang X, Chen M (2019) Nanoscale 11:7123–7128
28. Miao J, Xiao FX, Yang HB, Khoo SY, Chen J, Fan Z, Hsu YY, Chen HM, Zhang H, Liu B (2015) Sci Adv 1:e1500259
29. Kong X, Wang N, Zhang Q, Liang J, Wang M, Wei C, Chen X, Zhao Y, Zhang X (2018) ChemistrySelect 3:9493–9498
30. Lee WY, More KL (1995) J Mater Res 10:49–53
31. Li H, Zhang Q, Yap CCR, Tay BK, Edwin THT, Olivier A, Baillargeat D (2012) Adv Funct Mater 22:1385–1390
32. Balendhran S, Ou JZ, Bhaskaran M, Sriram S, Ippolito S, Vasic Z, Kats E, Bhargava S, Zhuiykov S, Zadeh KK (2012) Nanoscale 4:461–466
33. Ryu MY, Jang HK, Lee KJ, Piao M, Ko SP, Shin M, Huh J, Kim GT (2017) Phys Chem Chem Phys 19:13133–13139
34. Mignuzzi S, Pollard AJ, Bonini N, Brennan B, Gilmore IS, Pimenta MA, Richards D, Roy D (2015) Phys Rev B 91:195411
35. Kong D, Wang H, Cha JJ, Pasta M, Koski KJ, Yao J, Cui Y (2013) Nano Lett 13:1341–1347
36. Kibsgaard J, Chen Z, Reinecke BN, Jaramillo TF (2012) Nat Mater 11:963–969
37. Lin C, Gao Z, Jin J (2018) Chemsuschem 12:457. https://doi.org/10.1002/cssc.201802488
38. Wang H, Lu Z, Xu S, Kong D, Cha JJ, Zheng G, Hsu PC, Yan K, Bradshaw D, Prinz FB, Cui Y (2013) Proc Natl Acad Sci USA 110:19701–19706
39. Park GD, Cho JS, Kang YC (2015) Nanoscale 7:16781–16788
40. Conway BE, Tilak BV (2002) Electrochim Acta 47:3571–3594
41. Bolar S, Shit S, Kumar JS, Murmu NC, Ganesh RS, Inokawa H, Kuila T (2019) Appl Catal B: Environ 254:432–442
42. Qu Y, Yang M, Chai J, Tang Z, Shao M, Kwok CT, Yang M, Wang Z, Chua D, Wang S, Lu Z, Pan H (2017) ACS Appl Mater Interfaces 9:5959–5967
43. Han GQ, Li X, Xue J, Dong B, Shang X, Hu WH, Liu YR, Chi JQ, Yan KL, Chai YM, Liu CG (2017) Int J Hydrogen Energy 42:2952–2960

Affiliations

Cihan Kuru[1,3] · Mirac Alaf[1,3] · Yunus E. Simsek[2,3]

[1] Department of Metallurgical and Materials Engineering, Bilecik Seyh Edebali University, 11230 Bilecik, Turkey

[2] Department of Chemical Engineering, Bilecik Seyh Edebali University, 11230 Bilecik, Turkey

[3] Biotechnology Application and Research Centre, Bilecik Seyh Edebali University, 11230 Bilecik, Turkey